

## APPLICATION OF MODIFIED SUBJECTIVE SURFACE METHOD TO 3D CELL MEMBRANE IMAGE SEGMENTATION

MARKJOE OLUNNA UBA\* † , KAROL MIKULA\* , ZUZANA KRIVÁ\* , HANH NGUYEN‡ , THIERRY SAVY‡ , ELÉNA KARDASH‡ AND NADINE PEYRIÉRAS‡

**Abstract.** In this paper, we study 3D cell membrane image segmentation where the segmented surface is reconstructed by the use of 3D digital cell membrane image information and information that is obtained from thresholded 3D image in a local domain. The segmentation method is based on evolution of surface that is governed by a nonlinear PDE, the modified subjective surface equation. A semi-implicit finite volume scheme was used for the numerical discretization of the proposed model. The method was applied to real data representing 3D microscopy images of cell membrane within the zebrafish pectoral fin.

**Key words.** Image segmentation, subjective surface method, level set method, finite volume method, semi-implicit scheme, cell microscopy images, zebrafish.

**AMS subject classifications.** 65M08, 35K61, 68U10.

**1. Introduction.** Image segmentation is the process of subdividing the image domain into constituent parts. It is known to be one of the fundamental, difficult and most studied problems in image processing. There are many approaches to image segmentation (see e.g., [13, 6, 4, 2]) but in this paper, we focused on the subjective surface segmentation method. In image processing, this segmentation approach was introduced in [10, 11], studied and applied in [10, 11, 1, 8, 12, 14, 7]. Subjective surface segmentation method is based on the idea of segmentation function evolution that is governed by a geometrical diffusion model (see e.g., [12] and references contained therein for more details).

In applications, it is usually not easy to obtain optimal result using the subjective surface segmentation approach if the object that is intended to be segmented has internal structures or edges. The reason, may be attributed to the fact that this approach works with edge information throughout the process of segmentation. Hence, spurious edges or edges within the internal structures in an object of interest are also not disrespected during segmentation. For segmentation of membrane images which is the focus of this paper, the classical subjective surface segmentation approach seems not to give optimal result. This is, probably, as a result of the nature of membrane images. To improve the quality of the final segmentation result, we use the idea of local thresholding of image intensity values within a ball of appropriate radius around the approximate center of a membrane image. So, the idea is to presmooth the membrane image (to be segmented); apply the local thresholding to the presmoothed

---

\*Department of Mathematics and Descriptive Geometry, Faculty of Civil Engineering, Slovak University of Technology, Radlinskeho 11, 810 05 Bratislava, Slovakia (markjoeuba@gmail.com, karol.mikula@gmail.com, kriva@math.sk).

†Department of Mathematics, Faculty of Physical Sciences, University of Nigeria, 410001 Nsukka, Nigeria (markjoe.uba@unn.edu.ng).

‡BioEmergences Laboratory (FRE 2039), CNRS, University Paris-Saclay, 91190, Gif-sur-Yvette, France (thi.ngoc.hanh.nguyen@cnrs.fr, thierry.savy@gmail.com, Elena.KARDASH@cnrs.fr, nadine.peyrieras@cnrs.fr).

image; combine the information obtained from the thresholding with the information from the original membrane image intensities to get a segmentation result.

## 2. Main results.

**2.1. Mathematical model.** Let  $I^0 : \Omega \rightarrow \mathbb{R}$ ,  $\Omega \subset \mathbb{R}^3$  be the intensity function of a 3D membrane image. Let  $\alpha = \min_{x \in B(c,r)} G_\sigma * I^0(x)$ ,  $\beta = \max_{x \in B(c,r)} G_\sigma * I^0(x)$ , where  $G_\sigma$  is a smoothing kernel,  $B(c, r)$  is a ball with radius  $r$  centered at  $c$ , a given approximate central point inside the membrane image to be segmented. Then the threshold value which is used during the process of local thresholding may be chosen as  $t_r = \eta \alpha + (1 - \eta) \beta$ , with  $\eta \in [0, 1]$  and the ball radius may be chosen with respect to the approximate size of the membrane image to be segmented. So, the concept of local thresholding is to set all intensity values in the local neighborhood of center  $c$  to  $\beta$  if they are above  $t_r$  and  $\alpha$  otherwise.

Our method is based on solution of the following modification of subjective surface equation (see also [12])

$$(2.1) \quad u_t = |\nabla u| \nabla \cdot \left( G^0 \frac{\nabla u}{|\nabla u|} \right)$$

where  $G^0 = g(\delta |\nabla G_{\sigma_1} * I^0| + \theta |\nabla G_{\sigma_2} * I^{t_r}|)$ ;  $u$  is the unknown segmentation function;  $g$  is the Perona-Malik function typically defined as  $g(s) = \frac{1}{1+Ks^2}$ ;  $K > 0$  is a parameter chosen empirically [9];  $I^{t_r}$  is 3D image intensity of thresholded image within a ball of radius  $r > 0$ ;  $\delta, \theta \in [0, 1]$  determine the influence of information obtained from thresholding and membrane image intensities in the segmentation process;  $G_{\sigma_1}$  and  $G_{\sigma_2}$  are the smoothing kernels. Equation (2.1) go along with the following Dirichlet boundary conditions

$$(2.2) \quad u(t, x) = u^D \in [0, T] \times \partial\Omega,$$

and the initial condition

$$(2.3) \quad u(0, x) = u^0(x) \in \Omega.$$

$u^D$  is assumed without loss of generality to be 0. We note here that, if  $\delta = 1$  and  $\theta = 0$  then (2.1) reduces to the subjective surface segmentation model [10].

## 2.2. Numerical discretization.

**2.2.1. Time discretization.** Semi-implicit approach which is known to guarantee unconditional stability is used for time discretization of (2.1). Assume that equation (2.1) is solved in time interval  $I = [0, T]$  and  $N$  equal number of time steps. If the time step is denoted  $\tau = \frac{T}{N}$ , then the time discretization of (2.1) is given by

$$(2.4) \quad \frac{1}{\sqrt{\varepsilon^2 + |\nabla u^{n-1}|^2}} \frac{u^n - u^{n-1}}{\tau} = \nabla \cdot \left( G^0 \frac{\nabla u^n}{\sqrt{\varepsilon^2 + |\nabla u^{n-1}|^2}} \right),$$

where  $\varepsilon$  is a regularization parameter (Evans - Spruck [3]),  $u^0$  is given initial segmentation function, and  $u^n$ ,  $n = 1, \dots, N$  is the solution of the model in time step  $n$ .

**2.2.2. Space discretization.** For space discretization (see also, [12]), we used similar notations as those used in [8]. Although the step by step details of the discretization process is given in [12], for purpose of completeness we include these steps here also.

Let the finite volume mesh containing the voxels of 3D image be denoted  $\mathcal{T}_h$ , while  $V_{ijk}$ ,  $i = 1, \dots, N_1$ ,  $j = 1, \dots, N_2$ ,  $k = 1, \dots, N_3$  denote each finite volume. For each  $V_{ijk} \in \mathcal{T}_h$ , let  $h_1, h_2, h_3$  be the size of the volumes in  $x_1, x_2, x_3$  direction. Let the volume of  $V_{ijk}$  and its barycenter be denoted by  $m(V_{ijk})$  and  $c_{ijk}$  respectively. Let the approximate value of  $u^n$  in  $c_{ijk}$  be denoted by  $u_{ijk}^n$ . For every  $V_{ijk} \in \mathcal{T}_h$ , we denote the set of all  $(p, q, r)$  such that  $p, q, r \in \{-1, 0, 1\}$ ,  $|p| + |q| + |r| = 1$  by  $N_{ijk}$ , the set of all  $(p, q, r)$ ,  $p, q, r \in \{-1, 1\}$  by  $M_{ijk}$ , and the set of all  $(p, q, r)$  such that  $p, q, r \in \{-1, 0, 1\}$ ,  $|p| + |q| + |r| = 2$  by  $P_{ijk}$ . For each  $(p, q, r) \in N_{ijk}$ , denote the line connecting the center of  $V_{ijk}$  and the center of its neighbor  $V_{i+p, j+q, k+r}$  by  $\sigma_{ijk}^{pqr}$  and its length  $m(\sigma_{ijk}^{pqr})$ . We denote the planar sides, area and normal of finite volume  $V_{ijk}$  by  $e_{ijk}^{pqr}$ ,  $m(e_{ijk}^{pqr})$  and  $\nu_{ijk}^{pqr}$  respectively. Let  $x_{ijk}^{pqr}$  be the point of intersection of the line  $\sigma_{ijk}^{pqr}$  and planar side  $e_{ijk}^{pqr}$ . Furthermore, for each  $(p, q, r) \in M_{ijk}$ , let  $s_{ijk}^{pqr}$  denote the vertices of the finite volume  $V_{ijk}$ , and for each  $(p, q, r) \in P_{ijk}$ , let the midpoints of the voxel edges be denoted  $y_{ijk}^{pqr}$ . The approximate value of  $u^{n-1}$  in  $x_{ijk}^{pqr}$ ,  $y_{ijk}^{pqr}$  and  $s_{ijk}^{pqr}$ , with  $(p, q, r)$  belonging to the appropriate index set, is denoted by  $u_{ijk}^{pqr}$ ; the time index is omitted, as only the values from the time level  $n - 1$  will be needed at these points.

With these given notations, if we integrate (2.4) over finite volume  $V_{ijk}$ , we have that

$$(2.5) \quad \int_{V_{ijk}} \frac{1}{\sqrt{\varepsilon^2 + |\nabla u^{n-1}|^2}} \frac{u^n - u^{n-1}}{\tau} dx = \int_{V_{ijk}} \nabla \cdot \left( G^0 \frac{\nabla u^n}{\sqrt{\varepsilon^2 + |\nabla u^{n-1}|^2}} \right) dx.$$

Let the average value of  $A_\varepsilon = \sqrt{\varepsilon^2 + |\nabla u^{n-1}|^2}$  in finite volume  $V_{ijk}$  be denoted by  $\bar{A}_{\varepsilon,ijk}^{n-1}$ . Considering the fact that  $u^n$  and  $u^{n-1}$  are assumed to be piecewise constant over a finite volume mesh and using the divergence theorem we obtain that

$$(2.6) \quad m(V_{ijk}) \frac{u_{ijk}^n - u_{ijk}^{n-1}}{\tau} = \bar{A}_{\varepsilon,ijk}^{n-1} \sum_{N_{ijk}} \int_{e_{ijk}^{pqr}} G^0 \frac{\nabla u^n}{\sqrt{\varepsilon^2 + |\nabla u^{n-1}|^2}} \cdot \nu_{ijk}^{pqr} dS.$$

If the normal derivative  $\nabla u^n \cdot \nu_{ijk}^{pqr}$  is approximated by  $(u_{i+p, j+q, k+r}^n - u_{ijk}^n) / m(\sigma_{ijk}^{pqr})$  and  $A_{\varepsilon,ijk}^{pqr;n-1}$  and  $G_{ijk}^{pqr}$  are defined to be the averages of  $A_\varepsilon$  and  $G^0$  respectively on  $e_{ijk}^{pqr}$  then (2.6) reduces to

$$(2.7) \quad m(V_{ijk}) \frac{u_{ijk}^n - u_{ijk}^{n-1}}{\tau} = \bar{A}_{\varepsilon,ijk}^{n-1} \sum_{N_{ijk}} m(e_{ijk}^{pqr}) G_{ijk}^{pqr} \frac{u_{i+p, j+q, k+r}^n - u_{ijk}^n}{A_{\varepsilon,ijk}^{pqr;n-1} m(\sigma_{ijk}^{pqr})}.$$

Equation (2.7) simplifies to

$$(2.8) \quad u_{ijk}^n = u_{ijk}^{n-1} + \frac{\tau}{m(V_{ijk})} \bar{A}_{\varepsilon,ijk}^{n-1} \sum_{N_{ijk}} m(e_{ijk}^{pqr}) G_{ijk}^{pqr} \frac{u_{i+p, j+q, k+r}^n - u_{ijk}^n}{A_{\varepsilon,ijk}^{pqr;n-1} m(\sigma_{ijk}^{pqr})};$$

which further simplifies to

$$(2.9) \quad \left( 1 + \frac{\tau}{m(V_{ijk})} \bar{A}_{\varepsilon,ijk}^{n-1} \sum_{N_{ijk}} G_{ijk}^{pqr} \frac{m(e_{ijk}^{pqr})}{A_{\varepsilon,ijk}^{pqr;n-1} m(\sigma_{ijk}^{pqr})} \right) u_{ijk}^n - \frac{\tau}{m(V_{ijk})} \bar{A}_{\varepsilon,ijk}^{n-1} \sum_{N_{ijk}} G_{ijk}^{pqr} \frac{m(e_{ijk}^{pqr})}{A_{\varepsilon,ijk}^{pqr;n-1} m(\sigma_{ijk}^{pqr})} u_{i+p,j+q,k+r}^n = u_{ijk}^{n-1}$$

DEFINITION 2.1 (Global rescaling (see also, [12])). *Let  $\vartheta = \min_{\Omega} u_{ijk}^n$  and  $\zeta = \max_{\Omega} u_{ijk}^n$  for each time step  $n$ . Then the rescaled version of  $u_{ijk}^n$  given by (2.9) is obtained by the following relation  $u_{ijk}^n = \frac{1}{\zeta - \vartheta} (u_{ijk}^n - \vartheta)$ . As a result, we have that for each time step  $n$ , the rescaled version of  $u_{ijk}^n$  is in  $[0, 1]$  and it is used in the next time step.*

Equation (2.9) together with zero Dirichlet boundary condition, represents a system of linear equations which can be solved efficiently by the Successive Overrelaxation (SOR) method. Finally, we note how to determine the average values  $G_{ijk}^{pqr}$ ,  $A_{\varepsilon,ijk}^{pqr;n-1}$  and  $\bar{A}_{\varepsilon,ijk}^{n-1}$  either in voxels or on voxel sides. To determine these quantities, we used the reduced diamond cell strategy (see [8]). The idea of the reduced diamond cell approach is to drop the values in the eight corner points denoted by  $c_{i,j+q,k+r}$ ,  $c_{i+1,j+q,k+r}$ , with  $q, r \in \{-1, 1\}$  and as a result reducing the stencil from 18 to 10 points. Hence, from the computational standpoint, this approach reduces the computational cost.

Additionally, in the reduced diamond cell approach, the values of  $u^{n-1}$  are obtained from the midpoints  $y_{ijk}^{pqr}$  of the voxel edges. These values are given approximately for each  $(p, q, r) \in P_{ijk}$  by

$$\begin{aligned} u_{ijk}^{pq0} &= \frac{1}{4} \left( u_{ijk}^{n-1} + u_{i+p,j,k}^{n-1} + u_{i,j+q,k}^{n-1} + u_{i+p,j+q,k}^{n-1} \right), \\ u_{ijk}^{p0r} &= \frac{1}{4} \left( u_{ijk}^{n-1} + u_{i+p,j,k}^{n-1} + u_{i,j,k+r}^{n-1} + u_{i+p,j,k+r}^{n-1} \right), \\ u_{ijk}^{0qr} &= \frac{1}{4} \left( u_{ijk}^{n-1} + u_{i,j+q,k}^{n-1} + u_{i,j,k+r}^{n-1} + u_{i,j+q,k+r}^{n-1} \right). \end{aligned}$$

The components of the averaged gradient on  $e_{ijk}^{pqr}$  are approximated by 2D diamond cell approach in orthogonal planes which use the values  $u_{ijk}^{pqr}$  given above (see also [8]). This means that

$$\begin{aligned} \nabla^{p00} u_{ijk}^{n-1} &= \frac{1}{m(e_{ijk}^{p00})} \int_{e_{ijk}^{p00}} \nabla u^{n-1} dx \\ &\approx \left( p(u_{i+p,j,k}^{n-1} - u_{ijk}^{n-1})/h_1, (u_{ijk}^{p,1,0} - u_{ijk}^{p,-1,0})/h_2, (u_{ijk}^{p,0,1} - u_{ijk}^{p,0,-1})/h_3 \right), \end{aligned}$$

$$\nabla^{0q0} u_{ijk}^{n-1} = \frac{1}{m(e_{ijk}^{0q0})} \int_{e_{ijk}^{0q0}} \nabla u^{n-1} dx$$

$$\approx \left( (u_{ijk}^{1,q,0} - u_{ijk}^{-1,q,0})/h_1, q(u_{i,j,q,k}^{n-1} - u_{ijk}^{n-1})/h_2, (u_{ijk}^{0,q,1} - u_{ijk}^{0,q,-1})/h_3 \right),$$

$$\nabla^{00r} u_{ijk}^{n-1} = \frac{1}{m(e_{ijk}^{00r})} \int_{e_{ijk}^{00r}} \nabla u^{n-1} dx$$

$$\approx \left( (u_{ijk}^{1,0,r} - u_{ijk}^{-1,0,r})/h_1, (u_{ijk}^{0,1,r} - u_{ijk}^{0,-1,r})/h_2, r(u_{i,j,k+r}^{n-1} - u_{ijk}^{n-1})/h_3 \right).$$

Hence, we obtain that the approximations  $\nabla^{pqr} u_{ijk}^{n-1}$  for the gradient at the points  $x_{ijk}^{pqr}$ , with  $\nabla^{pqr} u_{ijk}^{n-1}$  denoting the approximation of the gradient in the barycenters  $x_{ijk}^{pqr}$  of voxel side  $e_{ijk}^{pqr}$ . Using the same approach for the computation of gradients of image intensities, the following approximations are obtained as well:

$$(2.10) \quad G_{ijk}^{pqr} = g \left( \delta |\nabla^{pqr} I_{\sigma_1;ijk}| + \theta |\nabla^{pqr} I_{\sigma_2;ijk}^{thr}| \right),$$

$$A_{\varepsilon,ijk}^{pqr;n-1} = \sqrt{\varepsilon^2 + |\nabla^{pqr} u_{ijk}^{n-1}|^2}, \quad \bar{A}_{\varepsilon,ijk}^{n-1} = \sqrt{\varepsilon^2 + \frac{1}{6} \sum_{N_{ijk}} |\nabla^{pqr} u_{ijk}^{n-1}|^2}.$$

**2.3. Numerical experiments.** In this section, numerical experiments were performed on biological image of a developing pectoral fin in zebrafish embryo in order to demonstrate the performance of our mathematical model (2.1) on membrane images. In all the experiments performed, isosurface 0.5 is displayed. 3D microscopy images of cell membrane were given to us to process by the research group of Nadine Peyri ras, (CNRS BioEmergences, France, in the framework of ImageInLife EC funded project). In zebrafish, pectoral fin serves as a vertebrate model for limb development. A sheet of cells converges at the prospective fin field location, subsequently proliferates and remodels into a 3D distinct structure. As the bud continues to grow and extends from the body trunk, cells undergo morphological changes to give rise to the fin 3D shape. Ectodermal cells are stretched and potentially play a part in shaping the fin while mesodermal cells decrease in volume in order to accommodate their neighbors given the increased compaction inside the fin. Here, we aim to measure dimensions of different cell types (EVL, ectoderm, lateral plate mesoderm, and somitic mesoderm) and monitor and quantify their shape changes influenced by external and internal forces during the 2D to 3D transition. To label cell nuclei and membrane globally, wild type zebrafish embryos were injected with mRNA encoding H2B-mCherry and eGFP-F at one-cell stage. Embryos were anesthetized and immobilized starting from 18 hours post fertilization and mounted on the upright confocal microscope Zeiss LSM 780. Datasets were acquired at the xy resolution of 0.6386660 m/pixel and 0.8467909 m/pixel z-direction. Nuclei centers were obtained using Difference of Gaussians algorithms and further validated using the software Mov-IT implemented in the Bioemergences Workflow[5]. The nuclei centers were used for construction of initial segmentation function in the presented membrane segmentation method.

We note that in all Figures 2.2–2.5, the first column shows the 3D volume rendering of the original 3D membrane image intensity and the second column shows, in black colour, their corresponding results after segmentation. Also, in Figure 2.1, first column of first row shows the 2D slice (along z axis) of 3D cell membrane image which

is intended to be segmented, first column of second row shows the 2D slice (along  $z$  axis) of 3D binarized image which is obtained by local thresholding, second column of first row shows the result of segmentation without local thresholding while second column of second row shows the result of segmentation with local thresholding. The partial reconstruction of the membrane image shown in second column of first row may be attributed to the fact that some internal structures or edges in the image did not allow the segmentation function to get to the actual boundary of the cell. However, with the local thresholding, the segmentation function is able to grow to the boundary of the cell giving rise to the result which is shown in second column of second row.

In the first numerical experiment,  $\delta = 1.0$  and  $\theta = 0.0$  were used. This choice of parameters reduced equation (2.1) to the classical subjective surface model [10]. Results obtained using these parameters are shown in Figures 2.2 and 2.4. Furthermore, for other numerical experiments,  $\delta = 0.8$  and  $\theta = 0.2$ ,  $\delta = 0.7$  and  $\theta = 0.3$ ,  $\delta = 0.6$  and  $\theta = 0.4$  were used. The results obtained using these parameters are shown in Figures 2.3 and 2.5. With these nonzero choices of  $\theta$ , it can be seen by visual comparison that the results are correct.

Finally, we note that in these numerical experiments, computations were done on a grid with  $50 \times 50 \times 40$  voxels, and computational method parameters were set to  $h = 0.01$ ,  $\tau = 0.01$ ,  $\eta = 0.95$ ,  $r = 26$ ,  $K = 0.8$  and  $N = 100$ .

In conclusion, it is not difficult to see that mathematical model (2.1) is a useful and successful generalization of the classical subjective surface model for 3D cell membrane image segmentation.

**Acknowledgments.** This work has received funding from the European Union's Horizon 2020 research and innovation programme under the Marie Skłodowska-Curie grant agreement No. 721537 and the project APVV-19-0460.

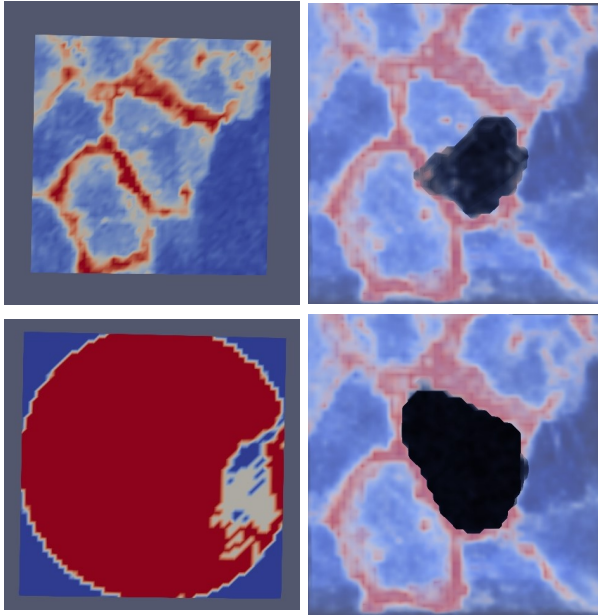


FIG. 2.1. In this figure, first column of first row shows the 2D slice (along  $z$  axis) of 3D cell membrane image which is intended to be segmented, first column of second row shows the 2D slice (along  $z$  axis) of 3D binarized image which is obtained by local thresholding, second column of first row shows the result of segmentation without local thresholding while second column of second row shows the result of segmentation with local thresholding.

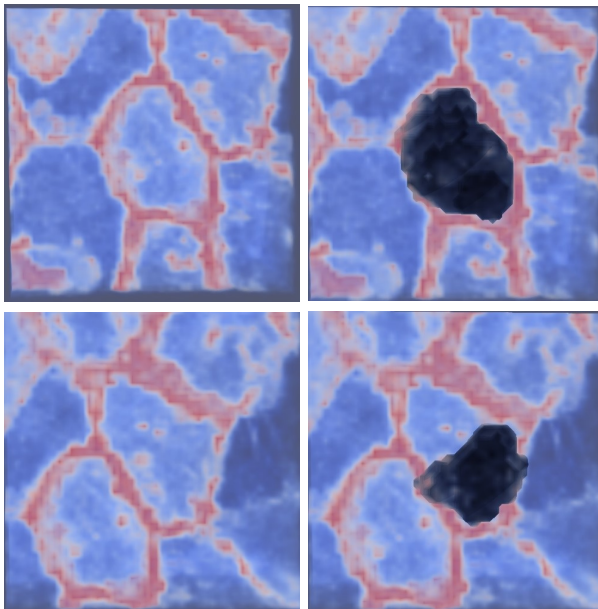


FIG. 2.2. First column of this figure shows the 3D volume rendering of the 3D cell membrane image which is intended to be segmented, while the second column shows the result after application of (2.1) with  $\delta = 1.0$  and  $\theta = 0.0$ .

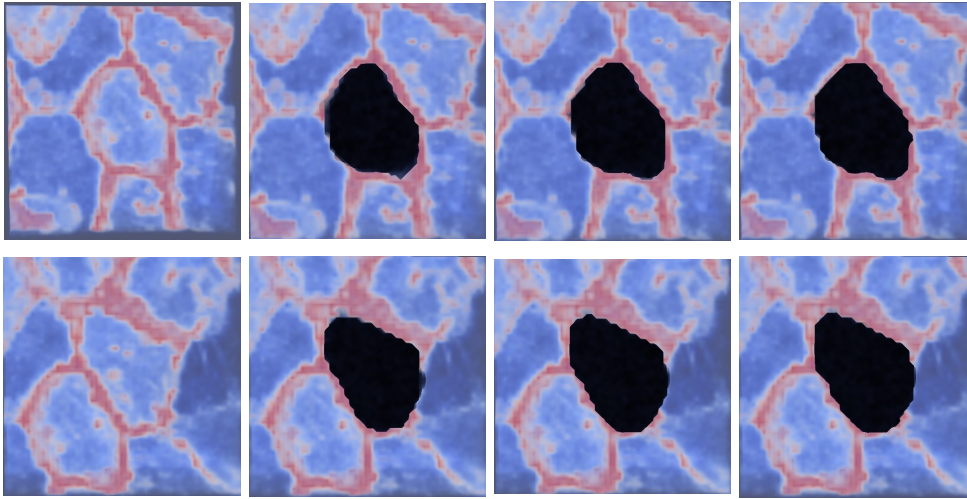


FIG. 2.3. First column of this figure shows the 3D volume rendering of the 3D cell membrane image which is intended to be segmented, while the second column shows the result after application of (2.1) with  $\delta = 0.8$  and  $\theta = 0.2$ ,  $\delta = 0.7$  and  $\theta = 0.3$ , and  $\delta = 0.6$  and  $\theta = 0.4$  respectively.

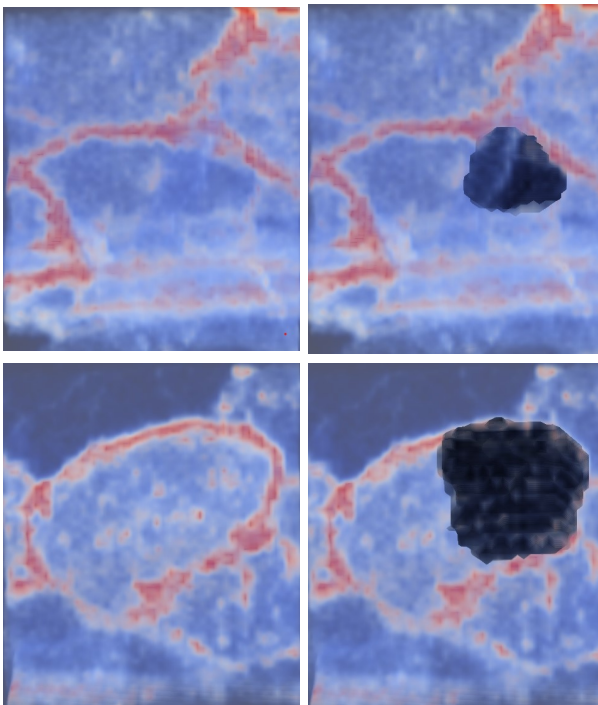


FIG. 2.4. First column of this figure shows the 3D volume rendering of the 3D cell membrane image which is intended to be segmented, while the second column shows the result after application of (2.1) with  $\delta = 1.0$  and  $\theta = 0.0$ .

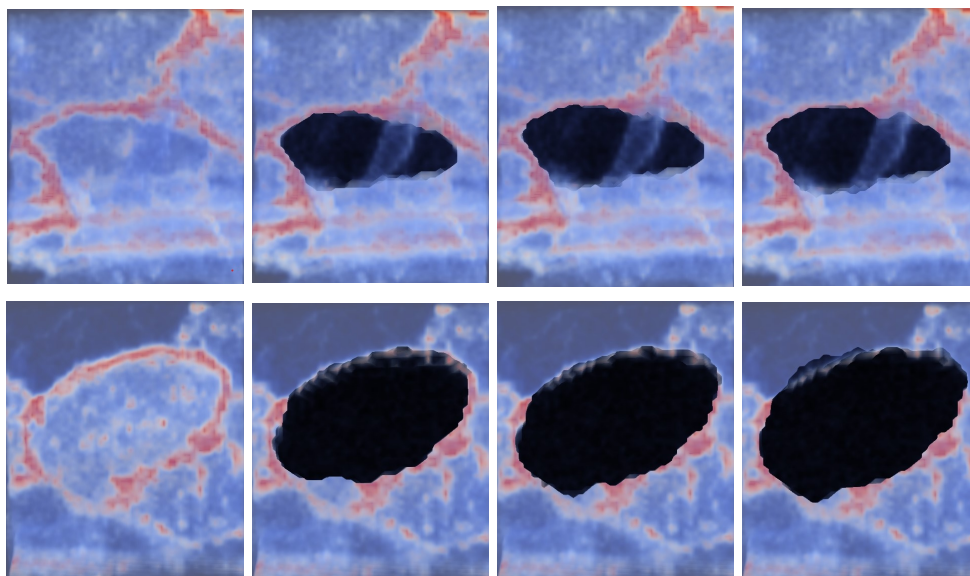


FIG. 2.5. First column of this figure shows the 3D volume rendering of the 3D cell membrane image which is intended to be segmented, while the second column shows the result after application of (2.1) with  $\delta = 0.8$  and  $\theta = 0.2$ ,  $\delta = 0.7$  and  $\theta = 0.3$ , and  $\delta = 0.6$  and  $\theta = 0.4$  respectively.

## REFERENCES

- [1] S. Corsaro, K. Mikula, A. Sarti, F. Sgallari, Semi-implicit co-volume method in 3D image segmentation, *SIAM J. Sci. Comput.*, vol. 28, num. 6, p. 2248-2265, 2006.
- [2] A. P. Dhawan, Image Segmentation, in *Medical Image Analysis*, *IEEE*, 2011, pp.229-264, doi:10.1002/9780470918548.ch10.
- [3] L. C. Evans and J. Spruck, Motion of level sets by mean curvature I, *J. Differential Geom.*, 33 (1991), 635–681. doi:10.4310/jdg/1214446559.
- [4] A. X. Falcao, J. K. Udupa, S. Samarasekera, S. Sharma, B. E. Hirsch, and R. de Alencar Lofufo, User-steered image segmentation paradigms: Live-wire and live-lane, *Graphics Models and Image Processing*, 60(4):223–260, 1998.
- [5] E. Faure, T. Savy, B. Rizzi, C. Melani, O. Drblíková, D. Fabregès, R. Špir, M. Hammons, R. Čunderlík, G. Recher, B. Lombardot, L. Duloquin, I. Colin, J. Kollár, S. Desnoullez, P. Affaticati, B. Maury, A. Boyreau, J. Nief, P. Calvat, P. Vernier, M. Frain, G. Lutfalla, Y. Kergosien, P. Suret, M. Remešíková, R. Doursat, A. Sarti, K. Mikula, N. Peyriéras, P. Bourguine, An algorithmic workflow for the automated processing of 3D+time microscopy imaging of developing organisms and reconstruction of their cell lineage, *Nature Communications*, 7 (2016), 8674.
- [6] M. Kass, A. Witkin, and D. Terzopoulos, Snakes: active contour models, *International Journal of Computer Vision*, 1(4):321-331, 1988.
- [7] K. Mikula, N. Peyriéras, M. Remešíková and O. Stašová Segmentation of 3D cell membrane images by PDE methods and its applications, *Computers in Biology and Medicine*, Vol. 41, No. 6 (2011) pp. 326-339.
- [8] K. Mikula and M. Remešíková, Finite volume schemes for the generalized subjective surface equation in image segmentation, *Kybernetika*, Vol. 45, No. 4 (2009) pp. 646-656.
- [9] P. Perona and J. Malik, Scale-space and edge detection using anisotropic diffusion, *IEEE Transactions on Pattern Analysis and Machine Intelligence*, 12 (1990), 629–639. doi:10.1109/34.56205.
- [10] A. Sarti, R. Malladi and J. A. Sethian, Subjective Surfaces: A Method for Completing Missing Boundaries, *PNAS*, Vol. 12, Num. 97, pp. 6258-6263, 2000.
- [11] A. Sarti, R. Malladi and J. A. Sethian, Subjective Surfaces: A Geometric Model for Boundary Completion, *International Journal of Computer Vision*, Vol. 46 Num. 3, pp. 201-221, 2002.
- [12] M. O. Uba, K. Mikula, Z. Krivá, H. Nguyen, T. Savy, E. Kardash, N. Peyriéras, 3D Cell Image

- Segmentation by Modified Subjective Surface Method, *Tatra Mountains Mathematical Publications*, (2020) 75, 147-162. doi: 10.2478/tmmp-2020-0010.
- [13] L. Vincent and P. Soille, Watersheds in Digital Spaces: an Efficient Algorithm Based on Immersion Simulations, *IEEE Transactions on Pattern Analysis and Machine Intelligence*, 13(6):583–598, 1991.
- [14] C. Zanella, M. Campana, B. Rizzi, C. Melani, G.Sanguinetti, P. Bourgine, K. Mikula, N. Peyri eras, A.Sarti, Cells Segmentation from 3-D Confocal Images of Early Zebrafish Embryogenesis, *IEEE Transactions on Image Processing*, Vol.19, No.3 (2010) pp. 770-781.